The Astrophysical Journal, 926:145 (8pp), 2022 February 20 https://doi.org/10.3847/1538-4357/ac4742

The MOSFIRE Deep Evolution Field Survey: Implications of the Lack of Evolution in the Dust Attenuation–Mass Relation to $z \sim 2$*

Alice E. Shapley[1], Ryan L. Sanders[2,11], Samir Salim[3], Naveen A. Reddy[4], Mariska Kriek[5,6], Bahram Mobasher[4], Alison L. Coil[7], Brian Siana[4], Sedona H. Price[8], Irene Shivaei[9], James S. Dunlop[10], Ross J. McLure[10], and Fergus Cullen[10]

[1] Department of Physics and Astronomy, University of California, Los Angeles, 430 Portola Plaza, Los Angeles, CA 90095, USA; aes@astro.ucla.edu
[2] Department of Physics, University of California, Davis, 1 Shields Avenue, Davis, CA 95616, USA
[3] Department of Astronomy, Indiana University, Bloomington, IN 47404, USA
[4] Department of Physics and Astronomy, University of California, Riverside, 900 University Avenue, Riverside, CA 92521, USA
[5] Astronomy Department, University of California at Berkeley, Berkeley, CA 94720, USA
[6] Leiden Observatory, Leiden University, NL-2300 RA Leiden, Netherlands
[7] Center for Astrophysics and Space Sciences, Department of Physics, University of California, San Diego, 9500 Gilman Drive, La Jolla, CA 92093, USA
[8] Max-Planck-Institut für Extraterrestrische Physik, Postfach 1312, Garching, D-85741, Germany
[9] Steward Observatory, University of Arizona, 933 N Cherry Avenue, Tucson, AZ 85721, USA
[10] Institute for Astronomy, University of Edinburgh, Royal Observatory, Edinburgh EH9 3HJ, UK
Received 2021 September 28; revised 2021 December 8; accepted 2021 December 29; published 2022 February 21

Abstract

We investigate the relationship between dust attenuation and stellar mass (M_*) in star-forming galaxies over cosmic time. For this analysis, we compare measurements from the MOSFIRE Deep Evolution Field survey at $z \sim 2.3$ and the Sloan Digital Sky Survey (SDSS) at $z \sim 0$, augmenting the latter optical data set with both UV Galaxy Evolution Explorer (GALEX) and mid-infrared Wide-field Infrared Survey Explorer (WISE) photometry from the GALEX-SDSS-WISE Catalog. We quantify dust attenuation using both spectroscopic measurements of Hα and Hβ emission lines, and photometric measurements of the rest-UV stellar continuum. The Hα/Hβ ratio is used to determine the magnitude of attenuation at the wavelength of Hα, $A_{\rm H\alpha}$. Rest-UV colors and spectral energy distribution fitting are used to estimate A_{1600}, the magnitude of attenuation at a rest wavelength of 1600 Å. As in previous work, we find a lack of significant evolution in the relation between dust attenuation and M_* over the redshift range $z \sim 0$ to $z \sim 2.3$. Folding in the latest estimates of the evolution of $M_{\rm dust}$, ($M_{\rm dust}/M_{\rm gas}$), and gas surface density at fixed M_*, we find that the expected $M_{\rm dust}$ and dust mass surface density are both significantly higher at $z \sim 2.3$ than at $z \sim 0$. These differences appear at odds with the lack of evolution in dust attenuation. To explain the striking constancy in attenuation versus M_*, it is essential to determine the relationship between metallicity and ($M_{\rm dust}/M_{\rm gas}$), the dust mass absorption coefficient and dust geometry, and the evolution of these relations and quantities from $z \sim 0$ to $z \sim 2.3$.

Unified Astronomy Thesaurus concepts: Galaxy evolution (594); High-redshift galaxies (734); Interstellar medium (847)

1. Introduction

Tracing the effects of dust attenuation on starlight is crucial for obtaining a complete census of star formation over cosmic time (e.g., Madau & Dickinson 2014). There are many different methods for quantifying the role played by dust in star-forming galaxies over a wide range in redshift. These rely on multiwavelength data probing the ratio of far-infrared (far-IR) to UV emission, i.e., reradiated versus unobscured starlight, and various measures of UV/optical reddening and/or attenuation. Measuring the dust content of star-forming galaxies over cosmic time in systems spanning a range of stellar and gas masses also places constraints on models for the formation and destruction of dust grains in the interstellar medium (ISM; e.g., Popping et al. 2017).

One particularly striking observation regarding dust in star-forming galaxies is that the relationship between dust attenuation and stellar mass (M_*) does *not* significantly evolve between $z \sim 0$ and $z \sim 2$ (and perhaps to even higher redshift). Here dust attenuation has been quantified as the ratio of far-IR to UV star formation rates (SFRs) or luminosities, which is also known as "IRX" (e.g., Meurer et al. 1999; Heinis et al. 2014; Bouwens et al. 2016; Bourne et al. 2017); the magnitude of far-UV (i.e., 1600 Å) attenuation, or A_{1600} (e.g., Pannella et al. 2015; McLure et al. 2018); the fraction of star formation that is obscured, $f_{\rm obscured}$ (Whitaker et al. 2017); and the nebular attenuation based on the Balmer decrement (i.e., Hα/Hβ ratio; Domínguez et al. 2013; Kashino et al. 2013; Price et al. 2014). There is less consensus regarding the form of the attenuation versus M_* relation at $z > 3$, with some evidence that it may evolve toward lower attenuation at fixed M_* (e.g., Fudamoto et al. 2020). However, at least out to $z \sim 2$, multiple results suggest a constant relation between dust attenuation and M_* in mass-complete samples (Whitaker et al. 2017; McLure et al. 2018).

* Based on data obtained at the W. M. Keck Observatory, which is operated as a scientific partnership among the California Institute of Technology, the University of California, and the National Aeronautics and Space Administration, and was made possible by the generous financial support of the W.M. Keck Foundation.
[11] Hubble Fellow.

The degree of dust attenuation in a galaxy reflects multiple key features of its ISM. First, there is the total dust content, $M_{\rm dust}$, and its relationship with the gas content of the galaxy, $M_{\rm gas}$. This dust content is intimately connected with the degree of metal enrichment in the galaxy, given that dust grains form from heavy elements (Rémy-Ruyer et al. 2014; De Vis et al. 2019). However, dust attenuation reflects not only the total dust content, $M_{\rm dust}$, but also its spatial distribution, which can be quantified in the most simplistic manner in terms of a characteristic radius, $r_{\rm dust}$ (i.e., a dust-continuum half-light radius). In more detail, the nonuniformity of the spatial distribution of dust must also be taken into account (e.g., Charlot & Fall 2000; Witt & Gordon 2000; Seon & Draine 2016). Finally, there is the question of the very properties of the dust grains, including their chemical composition, size distribution, and morphologies, which determines the relationship between $M_{\rm dust}$ and opacity.

Thus far, analyses of the (lack of) evolution in the attenuation versus M_* relation have not incorporated what is known about change in these other ISM components: $M_{\rm gas}$, metallicity ($12 + \log({\rm O/H})$, and $M_{\rm dust}$. Yet, they must be considered in order to gain a full understanding of why a measurement of M_* at $z \sim 0$ to $z \sim 2$ is so determinative of the degree of dust attenuation. Here, we analyze $z \sim 2.3$ dust attenuation based on rest-optical spectroscopic measurements of the Hα/Hβ Balmer decrement and rest-UV continuum measures of dust reddening. We also fold in independent results on the evolution of galaxy metallicities and gas and dust content, in order to gain a complete picture of the ISM of star-forming galaxies over the past ∼10 billion years. In Section 2, we describe our samples and observations. In Section 3, we present results on the observed relationship between dust attenuation and stellar mass at both $z \sim 2.3$ and $z \sim 0$. In Section 4, we discuss the surprising implications of the lack of strong evolution in the attenuation versus mass relation. Throughout, we adopt cosmological parameters of $H_0 = 70$ km s^{-1} Mpc^{-1}, $\Omega_m = 0.30$, and $\Omega_\Lambda = 0.7$, and a Chabrier (2003) initial mass function (IMF).

2. Sample and Observations

2.1. MOSFIRE Deep Evolution Field Survey

The analysis presented here is based on data from the MOSFIRE Deep Evolution Field (MOSDEF) survey, a large observing program using the Multi-Object Spectrometer for Infrared Exploration (MOSFIRE; McLean et al. 2012) on the 10 m Keck I telescope. As described in Kriek et al. (2015), with the MOSDEF survey we obtained rest-optical spectra for a sample of ∼1500 galaxies within three distinct redshift intervals spanning $1.4 \leqslant z \leqslant 3.8$. These intervals are $1.37 \leqslant z \leqslant 1.70$, $2.09 \leqslant z \leqslant 2.61$, and $2.95 \leqslant z \leqslant 3.80$, where the strongest rest-optical emission lines can be observed within windows of atmospheric transmission. MOSDEF targets fell in the COSMOS, GOODS-N, AEGIS, GOODS-S, and UDS fields, in regions covered by the CANDELS and 3D-HST surveys (Grogin et al. 2011; Koekemoer et al. 2011; Momcheva et al. 2016). These fields feature extensive multi-wavelength data sets spanning the electromagnetic spectrum, which can be used to infer a wide range of galaxy properties. The data used for fitting the spectral energy distributions (SEDs) of MOSDEF galaxies have been cataloged by the 3D-HST survey (Skelton et al. 2014), and include optical and near-IR ground-based and Hubble Space Telescope photometry, as well as Spitzer/IRAC mid-IR measurements. MOSDEF targets are selected based on existing photometric or spectroscopic redshifts, with a magnitude limit in the rest-optical (observed H band). This limit is $H_{\rm AB} = 24$, 24.5, and 25, respectively, for the lowest, middle, and highest redshift interval of the survey.

Here we focus on MOSDEF star-forming galaxies within the central target redshift range, i.e., $2.09 \leqslant z \leqslant 2.61$. Our $z \sim 2$ sample is very similar to the one analyzed in Sanders et al. (2021), with the additional constraint of $\geqslant 3\sigma$ detections of both Hα and Hβ line fluxes. Each galaxy has a robust estimate of nebular oxygen abundance ($12 + \log({\rm O/H})$) based on the subset of detected strong nebular emission lines drawn from [O II]$\lambda\lambda$3726, 3729, [Ne III]λ3869, Hβ, and [O III]λ5007 (at the very least [O II]$\lambda\lambda$3726, 3729, Hβ, and [O III]λ5007), as described in Sanders et al. (2021), and a measure of nebular dust attenuation ($A_{\rm H\alpha}$) based on the ratio Hα/Hβ and assuming the Cardelli et al. (1989) extinction law. We also estimated stellar masses by modeling the multiwavelength photometric SEDs cataloged by the 3D-HST team (Skelton et al. 2014), where the near-IR photometry was corrected for the contribution of strong nebular emission lines (Sanders et al. 2021). For SED modeling, we used the FAST (Kriek et al. 2009) program, assuming the stellar population synthesis models of Conroy et al. (2009), a Chabrier (2003) IMF, a Calzetti et al. (2000) dust law, and delayed-τ star formation histories, where ${\rm SFR}(t) \propto t\exp(-t/\tau)$. Here, t is the time since the onset of star formation and τ is the characteristic star formation timescale. We note that Balmer emission-line fluxes were corrected for the underlying stellar absorption implied by the best-fit stellar population model, with typical Balmer absorption corrections of ∼1% for Hα and ∼7% for Hβ. Finally, active galactic nuclei (AGNs) were identified and removed based on their X-ray and IR properties, as well as those with $\log([{\rm Ne\ II}]/{\rm H}\alpha) > -0.3$ (Coil et al. 2015; Azadi et al. 2017; Leung et al. 2019). In total, our MOSDEF sample includes 210 galaxies with a median redshift of $z_{\rm med} = 2.28$, a median stellar mass of $\log(M_*/M_\odot)_{\rm med} = 9.88$, and a median dust-corrected Hα-based SFR of ${\rm SFR}_{\rm med} = 29\ M_\odot\ {\rm yr}^{-1}$. These median properties are very well matched to those of the $z \sim 2.3$ sample analyzed in Sanders et al. (2021).

As an additional measure of dust attenuation, which probes the stellar continuum, we estimated the UV slope, β, directly from broadband photometry. β is calculated by fitting a power law of the form $f_\lambda \propto \lambda^\beta$ to the photometric bands spanning the rest-wavelength range 1268−2580 Å. This fit is typically determined based on 4−5 bands for galaxies in all fields except COSMOS, where the fit is typically based on 20 bands. The values of β were translated into estimates of rest-UV continuum attenuation (A_{1600}) for our sample based on a few different prescriptions. Following Reddy et al. (2018), and assuming an intrinsic stellar population from the Binary Population and Spectral Synthesis (BPASS) code (Eldridge et al. 2017), including binaries, an upper mass cut-off of $300\,M_\odot$, $Z_* = 0.02$, and $\log({\rm age/yr}) = 8.0$, we find the relation

$$A_{1600} = 2.13 \times \beta + 5.04 \quad (1)$$

for a Calzetti et al. (2000) dust-attenuation law, and

$$A_{1600} = 1.07 \times \beta + 2.52 \quad (2)$$

for an SMC extinction law (Gordon et al. 2003). We note that the relationship above for the Calzetti et al. (2000) law is based

on assuming an intrinsically bluer UV slope of $\beta_{\rm int} = -2.37$ for $z \sim 2$ star-forming galaxies than that found in earlier work for $z \sim 0$ starbursts. Specifically, in Meurer et al. (1999), the relationship between A_{1600} and β ($A_{1600} = 1.99 \times \beta + 4.43$) assumes an intrinsic UV slope of $\beta_{\rm int} = -2.23$. We also note that if BPASS models like the ones used to derive Equations (1) and (2) are adopted to estimate stellar masses, we obtain results extremely consistent with those based on FAST models. The same holds if we adopt the constant-star-formation, solar-metallicity models of Bruzual & Charlot (2003) to estimate stellar masses.

Recent results from the MOSDEF survey (Shivaei et al. 2020) suggest that a Calzetti et al. (2000)-type curve is appropriate at metallicities of $12 + \log({\rm O/H}) \geqslant 8.5$, while one resembling the SMC curve seems to apply at $12 + \log({\rm O/H}) < 8.5$. These results echo previous evidence from Reddy et al. (2010) and Reddy et al. (2012), that an SMC curve best describes the youngest (age $<$100 Myr) systems among a large sample of UV-selected galaxies at $z \sim 2$. Other recent work (e.g., McLure et al. 2018) has presented evidence that the Calzetti et al. (2000) curve applies over a wide range of stellar masses ($\log(M_*/M_\odot) \geqslant 9.75$), and, correspondingly, metallicities. Accordingly, our two favored methods for translating β into A_{1600} values for MOSDEF galaxies consist of (1) assuming the Calzetti et al. (2000) curve for the entire sample; (2) assuming the Calzetti et al. (2000) curve at $12 + \log({\rm O/H}) \geqslant 8.5$ and the SMC curve at $12 + \log({\rm O/H}) < 8.5$.

2.2. Sloan Digital Sky Survey Comparison Sample

In order to perform an evolutionary comparison, we selected a sample of local galaxies from the Sloan Digital Sky Survey (SDSS) Data Release 7 (DR7; Abazajian et al. 2009). Stellar masses and emission-line measurements corrected for stellar absorption were drawn from the MPA-JHU catalog of measurements for DR7.[12] In this catalog, SDSS stellar masses were estimated by fitting a grid of Bruzual & Charlot (2003) models spanning a wide range in star formation histories to u, g, r, i, and z emission-line-corrected photometry. We restricted the SDSS sample to galaxies at $0.04 \leqslant z \leqslant 0.10$ to reduce aperture effects, and, following Andrews & Martini (2013), required 5σ detections for [O II]$\lambda\lambda$3726, 3729, Hβ, Hα, and [Ne II]λ6584, and a 3σ detection for [O III]λ5007. We also removed galaxies satisfying the optical emission-line AGN criterion of Kauffmann et al. (2003), yielding a $z \sim 0$ comparison sample of 73,492 galaxies with $\log(M_*/M_\odot)_{\rm med} = 9.85$. The SDSS sample is very well matched to the $z \sim 2.3$ MOSDEF sample in terms of median stellar mass. However, the median SFR for the SDSS sample is ${\rm SFR}_{\rm med} = 1.3\,M_\odot$ yr^{-1}, i.e., a factor of $\sim$20 lower, which reflects the evolution of the star-forming main sequence (e.g., Förster Schreiber & Wuyts 2020, and references therein). Metallicities for SDSS galaxies were estimated using the calibrations presented in Figure 3 of Sanders et al. (2021), in order to provide the fairest comparison with respect to the $z \sim 2.3$ MOSDEF sample. Specifically, SDSS emission-line fluxes were corrected for the contribution of diffuse ionized gas (DIG) following Sanders et al. (2017), and then the combination of [O III]λ5007/Hβ and [O III]λ5007/[O II]$\lambda\lambda$3726, 3729 was fit simultaneously with the Sanders et al. (2021) $z \sim 0$ DIG-corrected metallicity calibrations to yield $12 + \log({\rm O/H})$.

In order to compare measures of rest-UV attenuation, we used the GALEX-SDSS-WISE Legacy catalog (GSWLC) presented in Salim et al. (2016). As described in Salim et al. (2016), UV/optical galaxy SEDs including Galaxy Evolution Explorer (GALEX) and SDSS photometry were modeled using the CIGALE code (Boquien et al. 2019), including two-component, exponentially declining star formation histories generated using Bruzual & Charlot (2003), and a range of dust-attenuation laws with varying UV slopes and UV-bump strengths. Constraints on the preferred dust law were obtained by forcing agreement between SED-based and mid-IR (from the Wide-field Infrared Survey Explorer; WISE) dust luminosities. One of the key outputs of the SED modeling using the GSWLC is the rest-UV attenuation, A_{1600}. GALEX near-UV and far-UV coverage is available for 30,204 galaxies in our SDSS comparison sample. We have confirmed that this GALEX subsample is representative of the larger SDSS-only sample, in terms of the relationship between Balmer line ratios and stellar mass (see Section 3).

3. Results

The relationship between attenuation and stellar mass has been considered using several different measures of the effects of dust. These include UV attenuation, A_{1600} (McLure et al. 2018), rest-optical continuum and line attenuation, A_V and $A_{\rm H\alpha}$ (Garn & Best 2010; Cullen et al. 2018), the ratio of FIR to UV luminosity, IRX (Heinis et al. 2014; Bourne et al. 2017), the fraction of star formation that is obscured, $f_{\rm obscured}$ (Whitaker et al. 2017), and the Balmer decrement (Domínguez et al. 2013; Kashino et al. 2013; Price et al. 2014). Here we analyze the attenuation of both rest-optical lines and rest-UV continuum as a function of stellar mass, and compare these relations for star-forming galaxies at $z \sim 0$ and $z \sim 2.3$.

First, we consider attenuation estimated from the ratio of Balmer emission lines, Hα/Hβ. Figure 1 (left) shows that there is a significant correlation between Hα/Hβ and M_*, such that higher Hα/Hβ ratios are associated with higher M_*. This correlation applies to both the $z \sim 0$ SDSS and $z \sim 2.3$ MOSDEF samples. We also plot the running median of Hα/Hβ in bins of M_*. The $z \sim 2.3$ running median relation between Hα/Hβ and M_* is entirely consistent with that of the $z \sim 0$ sample. The Hα/Hβ ratio can be translated into the nebular attenuation at the wavelength of Hα using a specific dust-extinction curve. For star-forming galaxies in the local universe, the Milky Way curve of Cardelli et al. (1989) is typically used to interpret nebular reddening. Recently, Reddy et al. (2020) demonstrated that the Cardelli et al. (1989) curve is also appropriate for dust-correcting nebular emission lines in MOSDEF galaxies at $1.4 \leqslant z \leqslant 2.6$. Using the Cardelli et al. (1989) curve for both $z \sim 0$ and $z \sim 2.3$ samples, we cast the Hα/Hβ versus M_* plot in terms of $A_{\rm H\alpha}$, the magnitude of nebular attenuation at the wavelength of Hα (Figure 1, right). As in the case of Hα/Hβ, the running medians of $A_{\rm H\alpha}$ in bins of M_* are also consistent between $z \sim 0$ and $z \sim 2.3$. We also note that the $z \sim 0$ relationship presented here between $A_{\rm H\alpha}$ and M_* is entirely consistent with that of Garn & Best (2010), when the same nebular attenuation law is assumed. Finally, the stacked $z \sim 1.6$ $A_{\rm H\alpha}$ measurements of Kashino et al. (2013), in three bins of M_*, are consistent with both our $z \sim 2.3$ and the

[12] Available at http://www.mpa-garching.mpg.de/SDSS/DR7/.

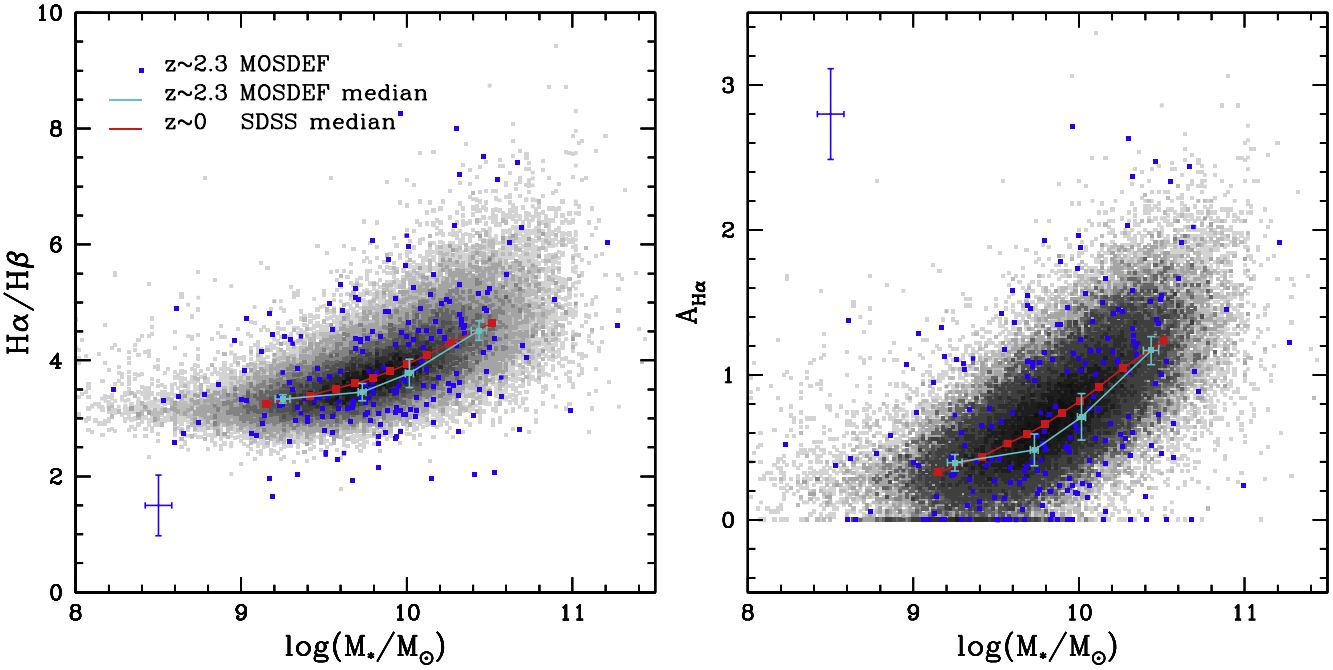

Figure 1. Attenuation vs. M_*, based on the Balmer line ratio, Hα/Hβ. In each panel, $z\sim2.3$ MOSDEF galaxies are indicated with blue points, and a median $z\sim2.3$ error bar is shown in the corner of the plot. The grayscale histogram corresponds to the distribution of local SDSS galaxies. Running median Hα/Hβ line ratios and the corresponding magnitude of attenuation at the wavelength of Hα, $A_{\rm H\alpha}$, are calculated in bins of stellar mass. The $z\sim2.3$ running median is indicated in turquoise, while that for SDSS is plotted in red. Median error bars are shown for the $z\sim2.3$ sample, while those for the SDSS sample are smaller than the symbols. Left: Hα/Hβ ratio vs. M_*. Right: $A_{\rm H\alpha}$ vs. M_*.

SDSS $z\sim0$ median relations in Figure 1, when the same stellar IMF and nebular attenuation law are assumed.

Dust attenuation is also commonly quantified in terms of its effect on the rest-UV stellar continuum. Such estimates of dust attenuation can be based on measurements of the UV slope, β, or else from SED fitting over a wider wavelength range. As described in Section 2.1, for the $z\sim2.3$ MOSDEF sample, we use measurements of β and either the Calzetti et al. (2000) dust curve at all metallicities (and masses), or else a metallicity-dependent dust curve (Calzetti et al. 2000 at high metallicity and SMC at low metallicity) to estimate A_{1600}. For the $z\sim0$ SDSS sample, A_{1600} is inferred from UV/optical SED fitting and energy balance considerations.

Figure 2 shows the relationship between A_{1600} and M_*. For the sake of simplifying the plot while still conveying key information, we do not display individual $z\sim2.3$ data points under different assumptions regarding the dust curve, but rather only the corresponding running medians. Over the full range in stellar mass, the $z\sim2.3$ and $z\sim0$ medians in A_{1600} are consistent within the errors when the Calzetti et al. (2000) curve is exclusively assumed (here, $z\sim2.3$ points are connected by a solid curve). In this case, the $z\sim2.3$ median A_{1600} values fall slightly higher than their $z\sim0$ counterparts at the same stellar mass. Our results are consistent with those of McLure et al. (2018), Equation (17), in the highest- and lowest-mass bins, though on average those authors find slightly higher A_{1600} at fixed mass than we do here. If we use a metallicity-dependent dust law to convert β to A_{1600} (here, $z\sim2.3$ points are connected by a dashed curve), the $z\sim2.3$ A_{1600} median values fall below the corresponding data points at $z\sim0$ and fixed stellar mass. The $z\sim2.3$ medians are consistent with those at $z\sim0$ down to a stellar mass of $\sim10^{10}\,M_\odot$ (at the $\sim0.4\sigma$ and 2.5σ level, respectively, for the highest and second-highest $z\sim2.3$ stellar mass bins). In the two lower-mass bins, the $z\sim2.3$ medians diverge downwards from the $z\sim0$ median curve at the 6.5–9.4σ level. For completeness, we also show the running median A_{1600} versus stellar mass at $z\sim2.3$ if the SMC dust curve is assumed for the entire sample (Reddy et al. 2018), in which case the $z\sim2.3$ sample running median A_{1600} falls significantly below the $z\sim0$ trend (here, $z\sim2.3$ points are connected by a dotted curve). However, we argue below that this final set of assumptions is inconsistent with other previous MOSDEF results. Based on the two more likely, bracketing, prescriptions for converting β to A_{1600} at $z\sim2.3$, we also infer no significant evolution from $z\sim0$ to $z\sim2.3$ in the relationship between A_{1600} and M_*.

It is worth emphasizing the distinct methodologies used for inferring A_{1600} at $z\sim0$ and $z\sim2.3$, each of which based on the available information at that redshift. In Figure 3, we show the relationship between A_{1600} and β for the $z\sim0$ SDSS sample, where β and A_{1600} are inferred from SED fitting spanning from the UV to optical, along with longer-wavelength energy balance considerations as described in Salim et al. (2016). Along with the running median A_{1600} for SDSS in bins of β, we overplot the relations from Equations (1) and (2) as two bracketing cases, along with the $z\sim0$ Calzetti relation from Meurer et al. (1999). The median SDSS relation falls in between those dictated by the Calzetti et al. (2000) and SMC curves, but significantly closer to the relationship traced by the SMC curve (see also Salim et al. 2018). Accordingly, while the SDSS sample is described by a wide range of dust-attenuation curves (Salim et al. 2016), on average these curves are steeper than the Calzetti et al. (2000) curve, and similar in UV slope to the SMC curve (Salim et al. 2018).

We do not have direct A_{1600} estimates for the majority of MOSDEF galaxies due to a lack of individual far-IR photometric detections, and rely on β measurements and the *assumption* of different dust curves to infer A_{1600}. At least

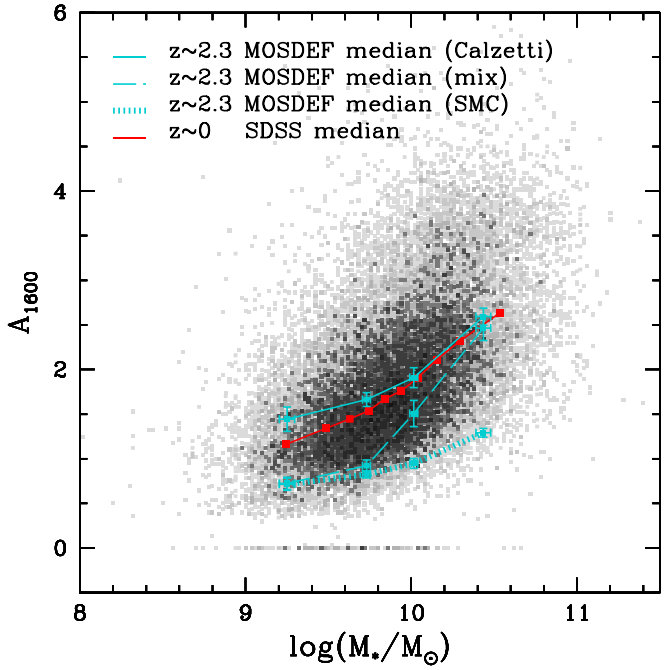

Figure 2. Attenuation vs. M_*, based on the rest-UV continuum. Here attenuation is quantified as A_{1600}, the magnitude of attenuation at a rest wavelength 1600 Å. As in Figure 1, the local SDSS sample is indicated as a gray histogram, and its running median A_{1600} estimated in bins of M_* is shown with red, connected symbols. A_{1600} is determined for SDSS galaxies as described in Salim et al. (2016). The running median A_{1600} for the $z \sim 2.3$ MOSDEF sample in bins of M_* is shown in turquoise, using three different prescriptions to translate the measured UV slope value, β, to A_{1600}. The solid curve shows A_{1600} based on assuming a Calzetti et al. (2000) dust-attenuation curve; the dashed curve shows A_{1600} assuming a Calzetti et al. (2000) curve at $12 + \log(\mathrm{O/H}) \geqslant 8.5$ and an SMC curve at $12 + \log(\mathrm{O/H}) < 8.5$; finally, the dotted curve shows A_{1600} assuming an SMC curve for the entire MOSDEF $z \sim 2.3$ sample (a scenario not favored by the MOSDEF data, but included for completeness). As in Figure 1, median error bars are shown for the $z \sim 2.3$ sample, while those for the SDSS sample are smaller than the symbols.

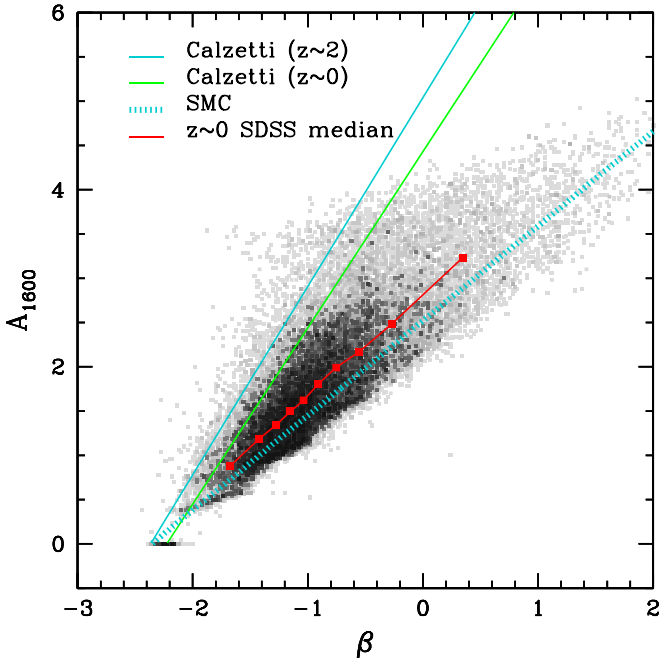

Figure 3. UV attenuation (A_{1600}) vs. UV slope β for local SDSS galaxies. The SDSS sample is indicated as a gray histogram, and its running median A_{1600} estimated in bins of β is shown with red, connected symbols. Also shown as bracketing cases are the expressions relating A_{1600} and β from Equations (1) and (2). The solid, turquoise line indicates the A_{1600}–β relation assuming the Calzetti et al. (2000) dust curve, while the dotted turquoise line shows the A_{1600}–β relation assuming the SMC dust curve. In addition, we show with a green, solid line the A_{1600}–β relation derived for $z \sim 0$ starbursts by Meurer et al. (1999). This relation is based on a slightly redder intrinsic UV slope than the one we have assumed for $z \sim 2$ star-forming galaxies and is consistent with the Calzetti et al. (2000) curve for $z \sim 0$ starbursts. The median relation between A_{1600} and β for SDSS galaxies, based on SED fitting and energy balance, more closely resembles that for an SMC dust curve than either Calzetti et al. (2000) relation, at least in the UV regime.

within the high-mass ($M_* \sim 10^{10}$–$10^{11}\,M_\odot$), high-SFR (30–250 $M_\odot$ yr^{-1}) range of the $z \sim 2.3$ MOSDEF sample, where Spitzer/MIPS, Herschel/PACS, and SPIRE detections have been achieved, SED fitting by Shivaei et al. (2016) suggests that the Calzetti et al. (2000; and not an SMC) law provides an accurate description of the energy balance between rest-frame UV and far-IR. Similar dust-continuum measurements are now required for lower-mass, lower-luminosity $z \sim 2.3$ MOSDEF galaxies, as in Reddy et al. (2018).

4. Discussion

We find no significant evolution in the relationship between dust attenuation and stellar mass between $z \sim 0$ and $z \sim 2.3$. Our results join a list of several that arrive at similar conclusions, based on different proxies for dust attenuation ($L_{\mathrm{IR}}/L_{\mathrm{UV}}$, or IRX; the fraction of obscured star formation, f_{obscured}; A_V; and A_{1600}) and different multiwavelength data sets (e.g., Heinis et al. 2014; Pannella et al. 2015; Bourne et al. 2017; Whitaker et al. 2017; Cullen et al. 2018; McLure et al. 2018). What is new here is the estimate of dust attenuation at $z \sim 2.3$ based on a large set of individual Balmer decrement measurements, as well as a direct comparison of UV attenuation, A_{1600}, at $z \sim 2.3$ and $z \sim 0$ based on GALEX data for the local SDSS comparison sample. As we now discuss, the lack of strong evolution in the attenuation versus stellar mass relation has striking implications, based on what else is known about the evolution of the ISM in star-forming galaxies between $z \sim 0$ and $z \sim 2.3$.

4.1. The Connection between Attenuation and other ISM Properties

We start with the expression for dust attenuation at a given wavelength, λ. For a given dust optical depth, τ_λ, and attenuation, A_λ, with the latter in magnitudes, we find

$$\exp(-\tau_\lambda) = 10^{-0.4A_\lambda}, \tag{3}$$

which corresponds to

$$A_\lambda = \frac{\tau_\lambda}{0.4\ln(10)} = 1.086 \times \tau_\lambda. \tag{4}$$

We then recall the expression for τ_λ, as a function of the dust mass absorption coefficient, κ_λ, in units of m^2 kg^{-1}, the dust density, ρ_{dust}, in units of kg m^{-3}, and the differential path length along the line of sight, ds:

$$\tau_\lambda = \int \kappa_\lambda \times \rho_{\mathrm{dust}}\, ds. \tag{5}$$

In a simplified model where κ_λ is spatially independent and dust is smoothly distributed throughout the galaxy disk, the integral can be reexpressed as the product of the dust mass absorption coefficient and the dust mass surface density,

$(M_{\rm dust}/(\pi r_{\rm dust}^2))$, where $M_{\rm dust}$ is the dust mass and $r_{\rm dust}$ is the scale of the disk over which dust is distributed:

$$\tau_\lambda \simeq \kappa_\lambda \times \left(\frac{M_{\rm dust}}{\pi r_{\rm dust}^2}\right). \quad (6)$$

Folding in Equation (4), we can express A_λ as a function of dust properties:

$$A_\lambda \simeq 1.086 \times \kappa_\lambda \times \left(\frac{M_{\rm dust}}{\pi r_{\rm dust}^2}\right). \quad (7)$$

Within the context of the simplified model presented here, the lack of significant evolution in A_λ at fixed stellar mass from $z \sim 0$ to $z \sim 2.3$ implies that the product $\kappa_\lambda \times (M_{\rm dust}/(\pi r_{\rm dust}^2))$ remains constant at fixed stellar mass.

4.1.1. Direct M_{dust} Measurements

First, we consider what is known from direct measurements of dust masses at high redshift. The Atacama Large Millimeter/submillimeter Array (ALMA) is now beginning to enable $M_{\rm dust}$ estimates for galaxies in the luminous end of the Luminous Infrared Galaxy (LIRG) regime (i.e., $10^{11}\,L_\odot \leqslant L_{\rm IR} \leqslant 10^{12}\,L_\odot$; Aravena et al. 2020; Shivaei et al. 2022), but does not yet cover the full range of stellar masses and SFRs in our sample. However, initial ALMA results from Magnelli et al. (2020) and Donevski et al. (2020) indicate signficant evolution in the $(M_{\rm dust}/M_*)$ ratio at fixed M_* from the local universe out to $z \sim 2$. Based on stacked measurements of galaxies covered by the ALMA Spectroscopic Survey (ASPECS) large program, Magnelli et al. (2020) find a best-fit factor of 10 evolution in $(M_{\rm dust}/M_*)$ for star-forming galaxies at a fiducial stellar mass of $M_* = 10^{10.7}\,M_\odot$ between $z = 0.45$ and $z = 2.0$. Likewise, for star-forming galaxies individually detected by ALMA, at a median redshift of $z_{\rm med} = 2.39$ and median stellar mass of $M_* = 10^{11}$, Donevski et al. (2020) find an order of magnitude increase in $(M_{\rm dust}/M_*)$ relative to that observed in the local galaxy sample of Andreani et al. (2018).

This observed evolution in $(M_{\rm dust}/M_*)$ exists in tension with model predictions from, e.g., Popping et al. (2017), which include a roughly constant relationship between $M_{\rm dust}$ and M_* over the redshift range $z \sim 0$ to $z \sim 2$. As highlighted by Popping et al. (2019), such models also significantly (by a factor of 2–3) underpredict the molecular gas content of $z \sim 2$ galaxies, which likely contributes to the discrepancy between their predicted and observed dust masses. The tension between the predicted and observed evolution of ISM gas and dust masses needs to be addressed.

4.1.2. The (M_{dust}/M_{gas}) Ratio and Gas Surface Density

We can also consider the question of evolution in A_λ by reexpressing the dust mass surface density, $(M_{\rm dust}/(\pi r_{\rm dust}^2))$, i.e., $\Sigma_{\rm dust}$, as the product $(M_{\rm dust}/M_{\rm gas}) \times \Sigma_{\rm gas}$. Here, $\Sigma_{\rm gas}$ is the gas surface density. Accordingly, we can rewrite Equation (7) as

$$A_\lambda \simeq 1.086 \times \kappa_\lambda \times \left(\frac{M_{\rm dust}}{M_{\rm gas}}\right) \times \Sigma_{\rm gas}. \quad (8)$$

With this equation, we can gain indirect constraints on the evolution of $\Sigma_{\rm dust}$ from estimates of the evolution of galaxy metallicity and gas surface density. For this analysis, we consider the evolution in galaxy properties at a fiducial stellar mass of $10^{10}\,M_\odot$, close to the median stellar mass of both the $z \sim 2.3$ MOSDEF and $z \sim 0$ SDSS samples.

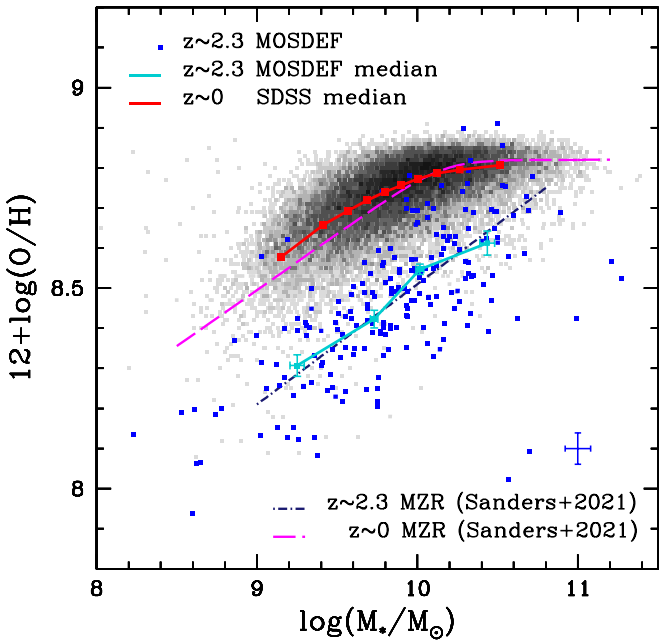

Figure 4. $12 + \log({\rm O/H})$ vs. M_*, i.e., the mass–metallicity relation (MZR). Symbols and running medians for $z \sim 2.3$ MOSDEF galaxies and local SDSS galaxies are as in Figure 1. $12 + \log({\rm O/H})$ is estimated for $z \sim 0$ and $z \sim 2.3$ galaxies following the prescriptions in Sanders et al. (2021). Also plotted are the best-fit $z \sim 0$ and $z \sim 2.3$ MZR relations from Table 3 of Sanders et al. (2021). The $z \sim 2.3$ best-fit relation exactly follows the running median $12 + \log({\rm O/H})$ in bins of M_*, while the $z \sim 0$ best-fit relation falls slightly below our running median at $\log(M_*/M_\odot) < 10$, due to small differences in SDSS comparison sample selection between the two works. At $M_* \sim 10^{10}\,M_\odot$, however, there is agreement between the best-fit SDSS MZR and our corresponding running median value. There is clear evolution toward lower $12 + \log({\rm O/H})$ at fixed M_*, which should be accompanied by a lower $(M_{\rm dust}/M_{\rm gas})$ according to the $(M_{\rm dust}/M_{\rm gas})$ vs. $12 + \log({\rm O/H})$ relation in De Vis et al. (2019).

In the first step, we can use the evolution in metallicity from $z \sim 0$ to $z \sim 2.3$ to infer the evolution in $(M_{\rm dust}/M_{\rm gas})$. As shown in Figure 4 and previous works (e.g., Steidel et al. 2014; Sanders et al. 2015, 2018, 2021), $z \sim 2.3$ galaxies have a lower metallicity at a fixed stellar mass relative to galaxies at $z \sim 0$. In addition to the local and $z \sim 2.3$ samples analyzed here, we plot the best-fit mass–metallicity relations from Sanders et al. (2021), which are consistent with our measurements and show that our dust-attenuation sample is representative of MOSDEF star-forming galaxies. The offset in metallicity is $\Delta 12 + \log({\rm O/H}) = 0.26 \pm 0.02$ dex toward lower metallicity at $z \sim 2.3$. This difference in metallicity can be translated into a reduction in $(M_{\rm dust}/M_{\rm gas})$ from $z \sim 0$ to $z \sim 2.3$ via the relationship between $(M_{\rm dust}/M_{\rm gas})$ and $12 + \log({\rm O/H})$. Most recently, De Vis et al. (2019) constructed this relationship for a large sample of local galaxies with $M_{\rm dust}$, $M_{\rm gas}$, and $12 + \log({\rm O/H})$ measurements. While the slope, a, of the relationship

$$\log\left(\frac{M_{\rm dust}}{M_{\rm gas}}\right) = a \times [12 + \log({\rm O/H})] + b \quad (9)$$

varies in detail depending on which empirical strong-line metallicity indictator is adopted, Table 4 of De Vis et al. (2019) shows that the values for a are distributed around 2. Shapley

et al. (2020) reported evidence for a lack of evolution in the $\log(M_{\rm dust}/M_{\rm gas})$ versus $12 + \log({\rm O/H})$ relationship, at least at the high-mass end ($10^{10.5}\,M_{\odot} \lesssim M_{*} \lesssim 10^{11}\,M_{\odot}$), and, therefore, we assume that the local relation can be applied to the $z \sim 2.3$ MOSDEF sample. Accordingly, we adopt a slope of $a = 2.0 \pm 0.2$ for the $(M_{\rm dust}/M_{\rm gas})$ versus $12 + \log({\rm O/H})$ relationship, and find that the decrease in $12 + \log({\rm O/H})$ implies a decrease of 0.52 ± 0.05 dex in $(M_{\rm dust}/M_{\rm gas})$ at fixed mass (i.e., a linear factor of 3.3 ± 0.4).

Next, we consider evolution in the gas surface density of star-forming galaxies out to $z \sim 2.3$. The molecular gas surface density evolves dramatically at fixed stellar mass over this redshift range. This evolution can be traced either by direct CO measurements (Tacconi et al. 2013), or else measurements of the change in SFR surface density, $\Sigma_{\rm SFR}$, coupled with an inversion of the Kennicutt–Schmidt (K-S) law. For example, based on the dust-corrected Hα SFRs and rest-optical half-light radii for both our $z \sim 2.3$ MOSDEF and $z \sim 0$ SDSS comparison samples, we find an increase of a factor of $\sim$65 in the median $\Sigma_{\rm SFR}$ (see also Shapley et al. 2019). Assuming a linear power-law slope for the K-S law (Tacconi et al. 2013), we infer an increase in molecular $\Sigma_{\rm gas}$ by the same factor of 65 from $z \sim 0$ to $z \sim 2.3$. While the gas content of $z \sim 2$ star-forming galaxies is well approximated by the molecular component (Tacconi et al. 2018), in local galaxies at the median stellar mass of our SDSS sample the molecular component only comprises $\sim$20% of the total molecular plus atomic gas mass (Catinella et al. 2018, Table 3). The evolution in total $\Sigma_{\rm gas}$ from $z \sim 0$ to $z \sim 2.3$ is therefore reduced by a factor of $\sim$5 relative to the inferred evolution in molecular $\Sigma_{\rm gas}$, since the total $\Sigma_{\rm gas}$ for $z \sim 0$ galaxies is a factor of $\sim$5 higher than the molecular component alone. Total $\Sigma_{\rm gas}$ is thus inferred to increase by a factor of $\sim$13. The net effect of the inferred evolution in $(M_{\rm dust}/M_{\rm gas})$ and $\Sigma_{\rm gas}$ is a factor of $(M_{\rm dust}/M_{\rm gas}) \times \Sigma_{\rm gas} \sim (1/3.3) \times 13$, i.e., a factor of $\sim$4. This factor corresponds to the increase in $\Sigma_{\rm dust}$, assuming that the spatial extent of dust and molecular gas is the same. ALMA has been used to obtain spatially resolved dust-continuum and CO maps for small samples of massive ($M_{*} > 10^{11}\,M_{\odot}$) and luminous ($L > 10^{12}\,L_{\odot}$) galaxies at $z \sim 2$ (Tadaki et al. 2017; Calistro Rivera et al. 2018; Kaasinen et al. 2020), but a clear picture has yet to emerge from these measurements regarding the relative extents of dust and molecular gas emission. A larger sample of spatially resolved measurements of both dust continuum and CO emission is required for less-luminous $z \sim 2.3$ main-sequence galaxies in the LIRG regime in order to understand if the extent of dust-continuum emission evolves in the same manner as that of the molecular gas.

4.2. Explaining the Lack of Evolution

In the extremely simplified picture presented in Section 4.1.1, in order to maintain a fixed attenuation, A_{λ}, at fixed stellar mass there must be evolution in either κ_{λ}, $r_{\rm dust}$, or both, in the sense that κ_{λ} is *smaller* and $r_{\rm dust}$ is effectively *larger* at $z \sim 2.3$ than at $z \sim 0$. Alternatively (or in addition), following the discussion in Section 4.1.2, if there is a stronger dependence of $(M_{\rm dust}/M_{\rm gas})$ on metallicity at $z \sim 2.3$ than at $z \sim 0$ (De Vis et al. 2019), such that a reduction of 0.26 dex in metallicity corresponds to a more extreme decrease in $(M_{\rm dust}/M_{\rm gas})$, this effect would also help to explain the lack of evolution in A_{λ} at fixed stellar mass. While additional data at lower metallicities is required to show the actual form of the relation at $z \sim 2.3$, initial results from Shapley et al. (2020) suggest that the normalization in the $(M_{\rm dust}/M_{\rm gas})$ versus $12 + \log({\rm O/H})$ relation does not evolve at solar metallicity.

We now consider one of the first two factors: the spatial extent of dust, $r_{\rm dust}$. Evolution in $r_{\rm dust}$ comprises another possibility for explaining the constant attenuation versus stellar mass relation in the face of significant $(M_{\rm dust}/M_{*})$ evolution. If $\pi r_{\rm dust}^2$ is a factor of $\sim$10 larger at $z \sim 2.3$ at fixed M_{*}, corresponding to an increase of a factor of $\sim$3 in $r_{\rm dust}$, then $(M_{\rm dust}/(\pi r_{\rm dust}^2))$ would remain constant. However, an evolution toward larger $r_{\rm dust}$ at higher redshift and fixed stellar mass is in conflict with both recent numerical simulations of galaxy formation including dust radiative transfer (Popping et al. 2022), as well as preliminary resolved ALMA measurements of the evolution of dust sizes. Specifically, Fujimoto et al. (2017) show for a sample of luminous ($L_{\rm FIR} \geqslant 10^{12}$) and massive ($\log(M_{*}/M_{\odot})_{\rm med} \sim 11$) galaxies drawn from the DANCING-ALMA survey that rest-frame far-IR sizes measured with ALMA (tracing dust continuum) decrease over the range $1.5 \leqslant z \leqslant 4$. Gómez-Guijarro et al. (2022) find a similar evolution toward smaller rest-frame far-IR continuum sizes as redshift increases over $z \sim 2$–4, based on GOODS-ALMA-2.0, a blind survey conducted at 1.1 mm covering a similar luminosity range. For a sample of four $z \sim 1.5$–2.0 galaxies with lower far-IR luminosities, in the LIRG range, Cheng et al. (2020) finds comparable $r_{\rm dust}$ values to those of local LIRGS from the KINGFISH (Kennicutt et al. 2011) and GOALS (Armus et al. 2009) surveys. However, there is no evidence to date for *larger* $r_{\rm dust}$ at higher redshift.

It may be that simply using an effective size, $r_{\rm dust}$, is insufficient to capture differences in the typical spatial distributions of dust at $z \sim 0$ and $z \sim 2.3$. For example, if dust distributions are patchier and clumpier at $z \sim 2$ than locally, the observed dust attenuation for a given $M_{\rm dust}$ will be lower (Witt & Gordon 2000; Seon & Draine 2016). Spatially resolved maps of dust-continuum emission extending up to $z \sim 2$ will be crucial for addressing this question. In addition, a detailed analysis of the shapes of dust-attenuation curves for galaxies of similar mass at low and high redshift can be used to determine the dust geometry indirectly in such systems (e.g., Chevallard et al. 2013).

One final possibility for explaining the constant attenuation versus stellar mass relation consists of evolution in κ_{λ}, the wavelength-dependent dust mass absorption coefficient. This dust cross-section per unit dust mass enscapsulates many different dust properties, including dust-grain size distribution, grain morphology, density, and chemical composition. Recently, Clark et al. (2019) empirically determined maps of κ_{λ} in two nearby face-on spiral galaxies. Clark et al. (2019) not only found significant variation of κ_{λ} within the individual galaxies targeted (see also Bianchi et al. 2019), but also that κ_{λ} is *inversely* correlated with gas surface density. Such an anticorrelation is not predicted by standard dust models, in which denser ISM regions are conducive to the growth of larger grains, which have higher emissivity (i.e., κ_{λ}) per unit mass. However, if lower κ_{λ} is generally associated with higher $\Sigma_{\rm gas}$, the significantly higher $\Sigma_{\rm gas}$ values at $z \sim 2.3$ described above may result in a lower κ_{λ} for these high-redshift galaxies than their low-redshift counterparts.

In summary, the roughly constant relationship between attenuation and stellar mass from $z \sim 0$ to $z \sim 2.3$ poses an

important puzzle, given the significant evolution in the gas and dust content of the ISM at fixed stellar mass over the same redshift range. We have highlighted multiple possiblities for explaining the lack of evolution in attenuation versus M_*. In particular, these include a steeper relationship between $(M_{\rm dust}/M_{\rm gas})$ and $12 + \log({\rm O/H})$ at $z \sim 2.3$, such that the decrease in $12 + \log({\rm O/H})$ translates into lower $(M_{\rm dust}/M_{\rm gas})$ at $z \sim 2.3$ than in the local universe; more extended dust distributions at $z \sim 2.3$ for galaxies at fixed stellar mass (though such a possibility seems inconsisent with both theory and preliminary observations), or, on the other hand, *clumpier* dust distributions at $z \sim 2.3$; and a lower dust mass absorption coefficient κ_λ. Directly measuring κ_λ at $z \sim 2.3$ seems beyond the reach of current facilities. However, determining $(M_{\rm dust}/M_{\rm gas})$ versus $12 + \log({\rm O/H})$ at subsolar metallicities, and obtaining spatially resolved maps of the dust-continuum emission for such galaxies is well within the scope of ALMA. Such observations should be highly prioritized in order to solve the puzzle of the nonevolving attenution versus stellar mass relation.

We acknowledge support from NSF AAG grant Nos. AST-1312780, 1312547, 1312764, 1313171, 2009313, and 2009085, grant No. AR-13907 from the Space Telescope Science Institute, grant No. NNX16AF54G from the NASA ADAP program, and the support of the UK Science and Technologies Facilities Council. Support for this work was also provided through the NASA Hubble Fellowship grant No. #HST-HF2-51469.001-A awarded by the Space Telescope Science Institute, which is operated by the Association of Universities for Research in Astronomy, Incorporated, under NASA contract NAS5-26555. We acknowledge helpful conversations with Ian Smail, Natascha Förster Schreiber, Tim Heckman, and John Peacock. We finally wish to extend special thanks to those of Hawaiian ancestry on whose sacred mountain we are privileged to be guests. Without their generous hospitality, the work presented herein would not have been possible.

ORCID iDs

Alice E. Shapley https://orcid.org/0000-0003-3509-4855
Ryan L. Sanders https://orcid.org/0000-0003-4792-9119
Samir Salim https://orcid.org/0000-0003-2342-7501
Naveen A. Reddy https://orcid.org/0000-0001-9687-4973
Mariska Kriek https://orcid.org/0000-0002-7613-9872
Alison L. Coil https://orcid.org/0000-0002-2583-5894
Brian Siana https://orcid.org/0000-0002-4935-9511
Sedona H. Price https://orcid.org/0000-0002-0108-4176
Irene Shivaei https://orcid.org/0000-0003-4702-7561
Fergus Cullen https://orcid.org/0000-0002-3736-476X

References

Abazajian, K. N., Adelman-McCarthy, J. K., Agüeros, M. A., et al. 2009, ApJS, 182, 543
Andreani, P., Boselli, A., Ciesla, L., et al. 2018, A&A, 617, A33
Andrews, B. H., & Martini, P. 2013, ApJ, 765, 140
Aravena, M., Boogaard, L., Gónzalez-López, J., et al. 2020, ApJ, 901, 79
Armus, L., Mazzarella, J. M., Evans, A. S., et al. 2009, PASP, 121, 559
Azadi, M., Coil, A. L., Aird, J., et al. 2017, ApJ, 835, 27
Bianchi, S., Casasola, V., Baes, M., et al. 2019, A&A, 631, A102
Boquien, M., Burgarella, D., Roehlly, Y., et al. 2019, A&A, 622, A103
Bourne, N., Dunlop, J. S., Merlin, E., et al. 2017, MNRAS, 467, 1360
Bouwens, R. J., Aravena, M., Decarli, R., et al. 2016, ApJ, 833, 72
Bruzual, G., & Charlot, S. 2003, MNRAS, 344, 1000
Calistro Rivera, G., Hodge, J. A., Smail, I., et al. 2018, ApJ, 863, 56
Calzetti, D., Armus, L., Bohlin, R. C., et al. 2000, ApJ, 533, 682
Cardelli, J. A., Clayton, G. C., & Mathis, J. S. 1989, ApJ, 345, 245
Catinella, B., Saintonge, A., Janowiecki, S., et al. 2018, MNRAS, 476, 875
Chabrier, G. 2003, PASP, 115, 763
Charlot, S., & Fall, S. M. 2000, ApJ, 539, 718
Cheng, C., Ibar, E., Smail, I., et al. 2020, MNRAS, 499, 5241
Chevallard, J., Charlot, S., Wandelt, B., & Wild, V. 2013, MNRAS, 432, 2061
Clark, C. J. R., De Vis, P., Baes, M., et al. 2019, MNRAS, 489, 5256
Coil, A. L., Aird, J., Reddy, N., et al. 2015, ApJ, 801, 35
Conroy, C., Gunn, J. E., & White, M. 2009, ApJ, 699, 486
Cullen, F., McLure, R. J., Khochfar, S., et al. 2018, MNRAS, 476, 3218
De Vis, P., Jones, A., Viaene, S., et al. 2019, A&A, 623, A5
Domínguez, A., Siana, B., Henry, A. L., et al. 2013, ApJ, 763, 145
Donevski, D., Lapi, A., Małek, K., et al. 2020, A&A, 644, A144
Eldridge, J. J., Stanway, E. R., Xiao, L., et al. 2017, PASA, 34, e058
Förster Schreiber, N. M., & Wuyts, S. 2020, ARA&A, 58, 661
Fudamoto, Y., Oesch, P. A., Magnelli, B., et al. 2020, MNRAS, 491, 4724
Fujimoto, S., Ouchi, M., Shibuya, T., & Nagai, H. 2017, ApJ, 850, 83
Garn, T., & Best, P. N. 2010, MNRAS, 409, 421
Gómez-Guijarro, C., Elbaz, D., Xiao, M., et al. 2022, A&A, 658, A43
Gordon, K. D., Clayton, G. C., Misselt, K. A., Landolt, A. U., & Wolff, M. J. 2003, ApJ, 594, 279
Grogin, N. A., Kocevski, D. D., Faber, S. M., et al. 2011, ApJS, 197, 35
Heinis, S., Buat, V., Béthermin, M., et al. 2014, MNRAS, 437, 1268
Kaasinen, M., Walter, F., Novak, M., et al. 2020, ApJ, 899, 37
Kashino, D., Silverman, J. D., Rodighiero, G., et al. 2013, ApJL, 777, L8
Kauffmann, G., Heckman, T. M., Tremonti, C., et al. 2003, MNRAS, 346, 1055
Kennicutt, R. C., Calzetti, D., Aniano, G., et al. 2011, PASP, 123, 1347
Koekemoer, A. M., Faber, S. M., Ferguson, H. C., et al. 2011, ApJS, 197, 36
Kriek, M., Shapley, A. E., Reddy, N. A., et al. 2015, ApJS, 218, 15
Kriek, M., van Dokkum, P. G., Labbé, I., et al. 2009, ApJ, 700, 221
Leung, G. C. K., Coil, A. L., Aird, J., et al. 2019, ApJ, 886, 11
Madau, P., & Dickinson, M. 2014, ARA&A, 52, 415
Magnelli, B., Boogaard, L., Decarli, R., et al. 2020, ApJ, 892, 66
McLean, I. S., Steidel, C. C., Epps, H. W., et al. 2012, Proc. SPIE, 8446, 84460J
McLure, R. J., Dunlop, J. S., Cullen, F., et al. 2018, MNRAS, 476, 3991
Meurer, G. R., Heckman, T. M., & Calzetti, D. 1999, ApJ, 521, 64
Momcheva, I. G., Brammer, G. B., van Dokkum, P. G., et al. 2016, ApJS, 225, 27
Pannella, M., Elbaz, D., Daddi, E., et al. 2015, ApJ, 807, 141
Popping, G., Pillepich, A., Calistro Rivera, G., et al. 2022, MNRAS, 510, 3321
Popping, G., Pillepich, A., Somerville, R. S., et al. 2019, ApJ, 882, 137
Popping, G., Somerville, R. S., & Galametz, M. 2017, MNRAS, 471, 3152
Price, S. H., Kriek, M., Brammer, G. B., et al. 2014, ApJ, 788, 86
Reddy, N., Dickinson, M., Elbaz, D., et al. 2012, ApJ, 744, 154
Reddy, N. A., Erb, D. K., Pettini, M., Steidel, C. C., & Shapley, A. E. 2010, ApJ, 712, 1070
Reddy, N. A., Oesch, P. A., Bouwens, R. J., et al. 2018, ApJ, 853, 56
Reddy, N. A., Shapley, A. E., Kriek, M., et al. 2020, ApJ, 902, 123
Rémy-Ruyer, A., Madden, S. C., Galliano, F., et al. 2014, A&A, 563, A31
Salim, S., Boquien, M., & Lee, J. C. 2018, ApJ, 859, 11
Salim, S., Lee, J. C., Janowiecki, S., et al. 2016, ApJS, 227, 2
Sanders, R. L., Shapley, A. E., Jones, T., et al. 2021, ApJ, 914, 19
Sanders, R. L., Shapley, A. E., Kriek, M., et al. 2015, ApJ, 799, 138
Sanders, R. L., Shapley, A. E., Kriek, M., et al. 2018, ApJ, 858, 99
Sanders, R. L., Shapley, A. E., Zhang, K., & Yan, R. 2017, ApJ, 850, 136
Seon, K.-I., & Draine, B. T. 2016, ApJ, 833, 201
Shapley, A. E., Cullen, F., Dunlop, J. S., et al. 2020, ApJL, 903, L16
Shapley, A. E., Sanders, R. L., Shao, P., et al. 2019, ApJL, 881, L35
Shivaei, I., Kriek, M., Reddy, N. A., et al. 2016, ApJL, 820, L23
Shivaei, I., Popping, G., Rieke, G., et al. 2022, arXiv:2201.04270
Shivaei, I., Reddy, N., Rieke, G., et al. 2020, ApJ, 899, 117
Skelton, R. E., Whitaker, K. E., Momcheva, I. G., et al. 2014, ApJS, 214, 24
Steidel, C. C., Rudie, G. C., Strom, A. L., et al. 2014, ApJ, 795, 165
Tacconi, L. J., Genzel, R., Saintonge, A., et al. 2018, ApJ, 853, 179
Tacconi, L. J., Neri, R., Genzel, R., et al. 2013, ApJ, 768, 74
Tadaki, K.-i., Kodama, T., Nelson, E. J., et al. 2017, ApJL, 841, L25
Whitaker, K. E., Pope, A., Cybulski, R., et al. 2017, ApJ, 850, 208
Witt, A. N., & Gordon, K. D. 2000, ApJ, 528, 799